



## Discrete geometry optimization for reducing flow non-uniformity, asymmetry, and parasitic minor loss pressure drops in Z-type configurations of fuel cells



Joshua M. Jackson <sup>a</sup>, Mateusz L. Hupert <sup>b</sup>, Steven A. Soper <sup>a, b, c, d, e,\*</sup>

<sup>a</sup> Department of Chemistry, UNC-Chapel Hill, NC, USA

<sup>b</sup> Department of Biomedical Engineering, UNC-Chapel Hill, NC, USA

<sup>c</sup> Department of Chemistry, LSU, Baton Rouge, LA, USA

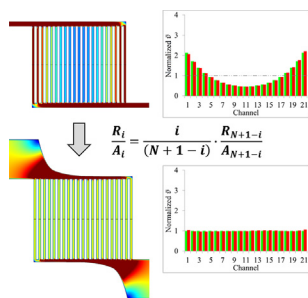
<sup>d</sup> Department of Mechanical Engineering, LSU, Baton Rouge, LA, USA

<sup>e</sup> Ulsan National Institute of Science and Technology, South Korea

### HIGHLIGHTS

- Algorithms for uniform flow distribution in Z-type fuel cells/stacks are derived.
- Simple equation shapes header structure to improve flow distribution.
- Reduced flow non-uniformity, flow asymmetry, and parasitic pressure.
- Rapidly applied to any Z-type geometry without affecting electroactive surfaces.

### GRAPHICAL ABSTRACT



### ARTICLE INFO

#### Article history:

Received 25 January 2014

Received in revised form

9 June 2014

Accepted 18 June 2014

Available online 7 July 2014

#### Keywords:

PEM fuel cell

Z-type configuration

Flow field

Flow distribution

Geometry optimization

### ABSTRACT

Parallel channel configurations, such as Z-type, used to distribute reagents in planar fuel cells provide lower overall pressure drop as compared to other channel designs. However, due to their inherent characteristics, flow maldistribution in parallel configurations is commonly observed and leads to starvation of reagents in middle channels. In addition, the Reynolds number dependent minor losses at branching tee junctions may cause asymmetric flow non-uniformity and reagent imbalance between the cathode and anode. Herein, we present a universal and simple optimization method to simultaneously reduce flow maldistribution, asymmetry, and parasitic pressure in Z-type parallel configurations of fuel cells or fuel cell stacks that has improved scalability relative to previous methods. A discrete model's governing equations were reduced to yield geometric ratios between headers. Increasing header widths to satisfy these ratios reduced flow maldistribution without modifying parallel channel geometry as validated by computation fluid dynamics (CFD) simulations. Furthermore, decreased Reynolds numbers throughout the headers reduced minor pressure drops and flow distribution asymmetry. We offer several methods to reduce the optimized geometry's footprint, including an adaptation of the discontinuous design.

© 2014 Elsevier B.V. All rights reserved.

\* Corresponding author. 116 Manning Dr., Mary Ellen Jones Building 906a, Chapel Hill, NC 27599, USA. Tel.: +1 919 845 5585; fax: +1 919 962 2388.

E-mail address: [ssoper@email.unc.edu](mailto:ssoper@email.unc.edu) (S.A. Soper).

## Nomenclature

$A$	cross-sectional area of channel ( $\text{m}^2$ )	$\Delta\Delta P$	change in pressure drop (Pa)
$a_i$	cross-sectional area of $i$ th parallel channel ( $\text{m}^2$ )	$R$	resistance ( $\text{kg m}^{-2} \text{s}^{-1}$ )
$a_p$	cross-sectional area of parallel channels ( $\text{m}^2$ )	$r_i$	resistance of $i$ th parallel channel ( $\text{kg m}^{-2} \text{s}^{-1}$ )
$A_i$	cross-sectional area of $i$ th inlet header ( $\text{m}^2$ )	$R_i$	resistance of $i$ th inlet header ( $\text{kg m}^{-2} \text{s}^{-1}$ )
$A'_i$	cross-sectional area of $i$ th outlet header ( $\text{m}^2$ )	$R'_i$	resistance of $i$ th outlet header ( $\text{kg m}^{-2} \text{s}^{-1}$ )
$A_{in}$	cross-sectional area of plate inlet ( $\text{m}^2$ )	$R_T$	resistance of tee junction ( $\text{kg m}^{-2} \text{s}^{-1}$ )
$A_T$	contact area of tee junction ( $\text{m}^2$ )	$Re$	Reynolds number
$D$	hydraulic diameter (m)	$U$	velocity field ( $\text{m s}^{-1}$ )
$F$	friction factor	$v_i$	velocity of $i$ th parallel channel ( $\text{m s}^{-1}$ )
$F_1$	non-uniformity index	$v_p$	velocity of parallel channels ( $\text{m s}^{-1}$ )
$F_2$	asymmetry index	$V_i$	velocity of $i$ th inlet header ( $\text{m s}^{-1}$ )
$F_\mu$	volumetric drag force ( $\text{N m}^{-3}$ )	$V'_i$	velocity of $i$ th outlet header ( $\text{m s}^{-1}$ )
$H$	channel height (m)	$V_{in}$	velocity of plate inlet ( $\text{m s}^{-1}$ )
$L$	channel length (m)	$W$	width (m)
$N$	number of channels	$W_i$	width of $i$ th inlet header (m)
$P$	channel perimeter (m)		
$\Delta P$	pressure drop (Pa)		

*Greek letters*

$\alpha$	aspect ratio
$\mu$	viscosity ( $\text{kg m}^{-1} \text{s}^{-1}$ )

## 1. Introduction

Proper design of gas distributors for planar fuel cells is critical to realize optimal operation and maximum power output of a fuel cell stack. To date, many flow designs have been proposed, evaluated, and are being used for reagent delivery in commercial fuel cells [1–4]. Among different configurations, two extremes can be defined: (i) A single serpentine channel covering the entire electrochemically active area of the fuel cell; and (ii) an array of parallel channels, herein focusing on designs with inlet and outlet channels arranged in the so-called Z-type configuration [1,5–7]. The serpentine channel provides the most uniform flow of reagents, but at the same time, suffers from the highest overall pressure drop. This is very undesirable for many high power systems with large electrode areas as the pump's power parasitically feeds from the fuel cell's power output [5]. On the other hand, parallel channel configurations offer the lowest pressure drop, as much as an order of magnitude lower than a serpentine channel covering the same area [8], but may suffer from severe flow maldistribution, where the middle channels are starved of reagent flow. This phenomenon can adversely affect a significant portion of the electroactive surface area and severely hampers power production of parallel-configured fuel cells [2–5,7–20].

While several methods have been developed to numerically predict the flow distribution of reagents in parallel configurations

[21], there are relatively few studies directed at reducing flow maldistribution by altering the Z-configuration's geometry [3,18,22–24]. As flow non-uniformity scales with the number of channels placed in parallel, various designs utilizing serially connected subsets of Z-geometries with fewer parallel channels, termed discontinuous geometries, have been proposed. However, applying a discontinuous parallel configuration typically increases parasitic pressure relative to a purely parallel design [3], and most critically, the fundamental non-uniform profiles remain even if they are reduced in magnitude. This last point was addressed by Zhang et al., who successfully corrected the non-uniform flow profiles in a Z-type configuration by adjusting the parallel channels' widths to increase flow through the middle channels [18]. However, this optimization method was presented in an ad hoc fashion as the authors did not provide a universal solution that can be applied to any geometry, an important point considering parameters vary from one study to the next. Moreover, Kumar, et al. [25] has shown that optimal geometric parameters exist for the electroactive channels [5]. Altering the widths of the parallel channels may evenly distribute reagent flow to the middle channels but at the expense of decreased reaction efficiency. In contrast, header widths have been adjusted to curb flow non-uniformity in Z-type [23] and pin-type [24] configurations, but to date, no universal equation has been presented to predict how header shape should be adjusted to

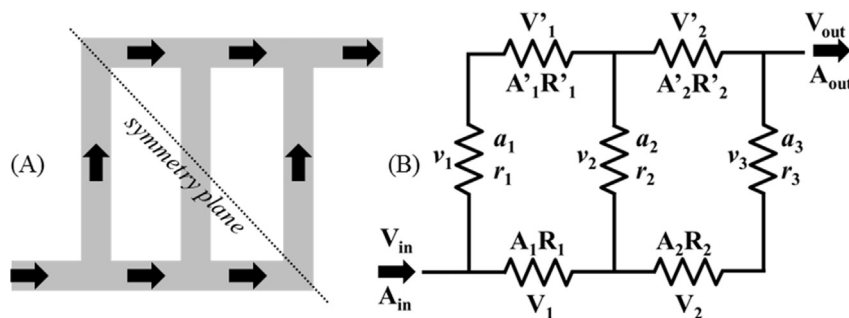


**Fig. 1.** (A) Schematic diagram and (B) discrete representation of a Z-configuration geometry. Arrows represent the direction of flow.

maximize flow uniformity in any Z-type design without the use of an optimization algorithm.

Herein, we present a simple and universal geometry optimization method to ensure uniform flow distribution in a Z-type fuel cell. We first generalize a discrete model (also termed a network analysis model) for Z-type configurations [18], where the geometry was subdivided into a network of individually defined fluidic resistors (see Fig. 1). The simplicity of such a model is desirable because pressure and mass balance equations may be defined and solved using only linear algebraic transformations of matrices, albeit these solutions are generally less descriptive than analytic methods or CFD simulations [18,26]. We exploit this simplicity to optimize the Z-configuration geometry by assuming the case where flow is perfectly distributed throughout the fuel cell and the geometric parameters of the parallel channels are constant. This permitted us to reduce the governing pressure and mass balance equations into straight forward geometric ratios between the inlet headers' resistances and areas that can be satisfied by increasing header widths using a simple algorithm, thereby offering superior scalability to previously demonstrated optimization algorithms [23,24]. We demonstrate this optimization process for several geometries and affirm the validity of these results by CFD simulation. This method comprised a simple yet effective approach for elucidating novel Z-type configurations of fuel cells, as well as fuel cell stacks, with markedly uniform flow distributions.

As an added benefit, the increased header widths reduce Reynolds numbers throughout the headers, thereby reducing flow recirculation in the branching tee junctions. In turn, this minimized asymmetric non-uniformity in reagent flow, parasitic minor loss pressure drops, and reagent imbalance between the cathode and anode, all of which have been detailed as concerns [3,22,26,27]. Furthermore, we provide avenues by which an optimized fuel cell's footprint can be reduced while retaining flow uniformity.

## 2. Computational methods

### 2.1. Assumptions

Both discrete and CFD models make the same assumptions: (1) The fluid's density ( $\rho$ ) and viscosity ( $\mu$ ) are constant; (2) temperature is held constant at 293.15 K; (3) the fluid flow is steady-state and laminar; and (4) mass transfer with the electrode layer is neglected [18,20].

### 2.2. Discrete model for Z-configuration geometries

We adopted a discrete model [18] in which a Z-type configuration fuel cell was segmented into a system of individual, interconnected fluidic resistors as seen in Fig. 1. A channel segment's geometry dictates resistance ( $R$ ) to fluid flow by;

$$R = \frac{1}{2} \frac{(Re f)\mu PL}{DA} \quad (1)$$

where the channel's geometry is defined by its cross-sectional area ( $A$ ), perimeter ( $P$ ), length ( $L$ ), width ( $W$ ), and height ( $H$ ). The hydraulic diameter ( $D$ ) is given by  $4WH/2(W+H)$ , and the product of the Reynolds number and friction factor ( $Re f$ ) is approximated by Kays and Crawford [28] as  $13.84 + 10.38\exp(-3.4/\alpha)$ , where  $\alpha$  is the channel's aspect ratio ( $\geq 1$ ). Additionally, merging the parallel channels and header segments in a tee junction implicitly adds a

resistance term ( $R_T$ ) to a header segment due to the contact area of the tee junction ( $A_T$ ):

$$R_T = \frac{1}{2} \frac{(Re f)\mu A_T}{DA} \quad (2)$$

In Eq. (2), all geometric parameters take into account the associated header segment [18]. Also note that this model neglects any added tee junction resistance term to the parallel channels due to their length. This assumption is addressed in Section 6.

Using the resultant resistances, we can solve a set of pressure and mass balance equations to determine the flow distribution through the parallel channels of a Z-configuration fuel cell. The pressure and mass balance equations for the Z-configuration presented in Fig. 1 are as follows:

$$v_1 r_1 + V'_1 R'_1 = V_1 R_1 + v_2 r_2 \quad (3a)$$

$$v_2 r_2 + V'_2 R'_2 = V_2 R_2 + v_3 r_3 \quad (3b)$$

$$V_{in} A_{in} = V_1 A_1 + v_1 a_1 \quad (3c)$$

$$V_1 A_1 = V_2 A_2 + v_2 a_2 \quad (3d)$$

$$V_2 A_2 = v_3 a_3 \quad (3e)$$

$$V_{in} A_{in} = V_1 A_1 + V'_1 A'_1 = V_2 A_2 + V'_2 A'_2 \quad (3f)$$

where  $v_i$ ,  $r_i$ , and  $a_i$  are the average linear velocity, resistance, and cross-sectional area of the  $i$ th parallel channel. Similarly,  $V_i$ ,  $R_i$ , and  $A_i$  describe the  $i$ th inlet header segment, and  $V'_i$ ,  $R'_i$ , and  $A'_i$  correspond to the  $i$ th outlet header segment.

Because each segment is independently defined, it is relatively straightforward to extend the geometry in Fig. 1 to a system with  $N$  parallel channels and  $N - 1$  inlet and outlet header segments. Moreover, we express Eq. (3) in matrix form so that a custom computer algorithm can be used to solve for the system's average linear velocities and flow distribution. For brevity, we apply both transformations simultaneously and find the following;

$$[M] = [R][V] \quad (4a)$$

where

$$[M] = \begin{bmatrix} -\frac{V_{in} R'_1 A_{in}}{A'_1} \\ -\frac{V_{in} R'_2 A_{in}}{A'_2} \\ \vdots \\ -\frac{V_{in} R'_{N-1} A_{in}}{A'_{N-1}} \\ A_{in} V_{in} \\ 0 \\ \vdots \\ 0 \end{bmatrix} \quad (4b)$$

$$[R] = \begin{bmatrix} r_1 & -r_2 & 0 & 0 & \dots & 0 & -\left(R_1 + \frac{R'_1 A_1}{A'_1}\right) & 0 & 0 & \dots & 0 \\ 0 & r_2 & -r_3 & 0 & \dots & 0 & 0 & -\left(R_2 + \frac{R'_2 A_2}{A'_2}\right) & 0 & \dots & 0 \\ \vdots & \vdots & \ddots & \ddots & \ddots & \vdots & \vdots & \ddots & \ddots & \ddots & \vdots \\ 0 & 0 & \dots & 0 & r_{N-1} & -r_N & 0 & 0 & \dots & 0 & -\left(R_{N-1} + \frac{R'_{N-1} A_{N-1}}{A'_{N-1}}\right) \\ a_1 & 0 & 0 & 0 & \dots & 0 & A_1 & 0 & \dots & \dots & 0 \\ 0 & a_2 & 0 & 0 & \dots & 0 & -A_1 & A_2 & \dots & \ddots & \vdots \\ 0 & 0 & a_3 & 0 & \dots & 0 & 0 & -A_2 & \dots & \ddots & \vdots \\ \vdots & \vdots & \ddots & \ddots & \ddots & \vdots & \vdots & 0 & \ddots & \ddots & 0 \\ 0 & 0 & \dots & \dots & a_{N-1} & 0 & \vdots & \vdots & \dots & -A_{N-2} & A_{N-1} \\ 0 & 0 & \dots & \dots & 0 & a_N & 0 & 0 & \dots & 0 & -A_{N-1} \end{bmatrix} \quad (4c)$$

$$[V] = \begin{bmatrix} v_1 \\ v_2 \\ \vdots \\ v_N \\ V_1 \\ V_2 \\ \vdots \\ V_{N-1} \end{bmatrix} \quad (4d)$$

Note that the matrices in Eq. (4b and c) reduce to those published by Zhang et al. [18] if the proper substitutions are made.

We constructed an algorithm using the FORTRAN 77 programming language to solve Eq. (4). Using any set of fluidic and geometric parameters, the program automatically assembled the [M] and [R] matrices using Eq. (4b and c) and inverted the [R] matrix to form the  $[R]^{-1}$  matrix. The stability of this inversion was tested by outputting the diagnostic  $\det([R][R]^{-1}) = \det([I])$ , which was unity for systems where  $N = 1000$ . Finally,  $[R]^{-1}[M]$  was computed to give the [V] matrix in Eq. (4d). The first  $N$  elements of the [V] matrix yielded the flow distribution throughout their parallel channels of the specified Z-configuration geometry, which was characterized by an established non-uniformity index [8,12]:

$$F_1 = \frac{\max(v_1 \dots v_N) - \min(v_1 \dots v_N)}{\max(v_1 \dots v_N)} \quad (5)$$

In the case of perfectly uniform distribution,  $F_1 = 0$ , and  $F_1 \rightarrow 1$  as flow non-uniformity becomes increasingly severe.

### 2.3. Discrete geometry optimization

To optimize a Z-type parallel configuration of a fuel cell for flow uniformity, we must make a few assumptions. First, we assume that

the flow is perfectly distributed through the parallel channels, i.e.,  $v_1 \dots v_N = v_P$  in Eqs. (3a–e). We then recognize that the pressure balance equations in Eq. (3a and b) simplify to;

$$V_i R_i = V'_i R'_i \quad (6a)$$

and the mass-balance equations in Eqs. (3c–e) imply that;

$$V_N A_N = v_P a_P \quad (6b)$$

$$V_{N-1} A_{N-1} = V_N A_N + v_P a_P = 2v_P a_P \quad (6c)$$

which can be generalized for the  $i$ th inlet header by;

$$V_i = (N + 1 - i) \cdot \frac{a_P v_P}{A_i} \quad (6d)$$

We now make a second assumption that the entire Z-configuration is symmetric (symmetry plane shown in Fig. 1A). Here, the geometry of the  $i$ th inlet header is identical to the  $(N - i)$ th outlet header. For the geometry in Fig. 1, this means that  $A_1 = A_3'$  and  $A'_1 = A_3$ , which is also true for widths, heights, resistances, and average velocities. By Eq. (6a), this constraint immediately leads to a universal set of solutions by relating the  $i$ th and  $(N + 1 - i)$ th inlet headers;

$$V_i R_i = V'_i R'_i = V_{N+1-i} R_{N+1-i} \quad (6e)$$

We then substitute Eq. (6d) on both sides of Eq. (6e) to give;

$$(N + 1 - i) \cdot \frac{a_P v_P R_i}{A_i} = i \cdot \frac{a_P v_P R_{N+1-i}}{A_{N+1-i}} \quad (7)$$

which reduces to

**Table 1**

Non-optimized geometric parameters (units: mm),  $F_1$  parameters from discrete and CFD results, CFD pressure drops (units: Pa), and references for geometries I–III.

Geometry	Discrete			Parallel channel properties				Rib width	Inlet width	Inlet height	Ref.
	$F_1$	$F_1$	$\Delta P$	Number	Length	Width	Height				
I	0.40	0.41	11.1	11	50.00	1.50	0.60	1.50	3.00	0.60	[18]
II	0.78	0.79	30.1	21	50.00	1.50	0.60	1.50	3.00	0.60	[18]
III	0.92	0.92	39.6	26	50.00	2.00	0.72	2.00	4.00	0.72	[8]

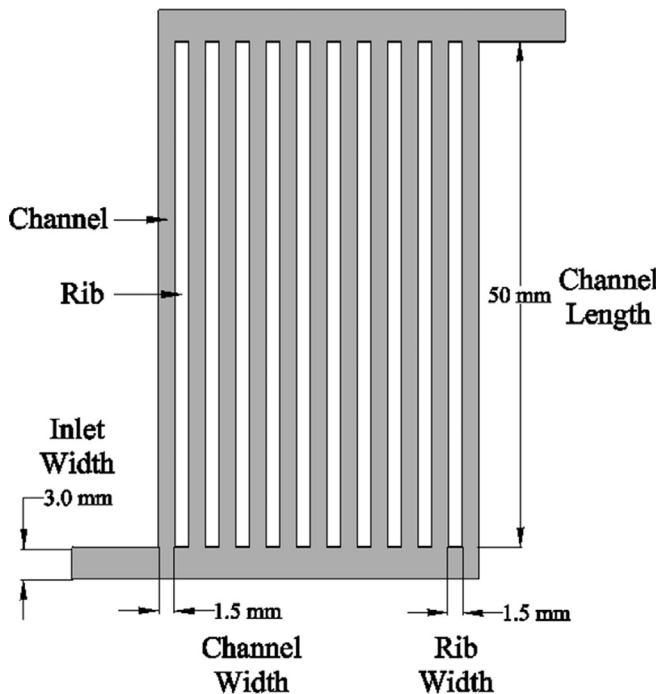


**Fig. 2.** Labeled drawing of geometry I. Refer to Tables 1 and 3 for all parameters of geometries I–III and IV–V, respectively.

$$\frac{R_i}{A_i} = \frac{i}{(N+1-i)} \cdot \frac{R_{N+1-i}}{A_{N+1-i}} \quad (8)$$

The  $R/A$  ratio for a header segment is given by simplification of Eqs. (1) and (2);

$$\frac{R}{A} = \frac{\mu L \left( 13.84 + 10.38 \cdot e^{-\frac{3.4W}{H}} \right) (W+H)^2}{2 \cdot W^3 H^3} + \frac{\mu A_T \left( 13.84 + 10.38 \cdot e^{-\frac{3.4W}{H}} \right) (W+H)}{4 \cdot W^3 H^3} \quad (9)$$

assuming that the segment's aspect ratio is given by  $W/H$ , i.e.,  $W/H \geq 1$ .

Eq. (8) is the key to our optimization method because it relates the first  $1\dots N/2$  inlet headers to the last  $N/2\dots N-1$  inlet headers. Practically, we can change the dimensions of the  $1\dots N/2$  inlet headers with respect to the  $N/2\dots N-1$  inlet headers to satisfy Eq. (8). It is entirely possible to vary header heights to satisfy Eq. (8), but this approach could generate several problems. If the parallel channels heights are not altered to match the header heights, reagent must flow over an additional surface from deeper inlet headers to shallower parallel channels, and this could induce significant minor losses at higher Reynolds numbers similar to those observed in Section 6 of this publication and unknown effects on the flow distribution. However, if the parallel channel heights are altered, this could negatively impact optimal power generation in the parallel channels as shown by Kumar et al. [5,25]. Therefore, we chose to alter the headers' widths to satisfy Eq. (8).

There are infinite solutions to the outlined  $R/A$  relationships; some constraint must be emplaced to arrive at a unique solution, which we arbitrarily assigned as a minimized footprint herein. Thus, we begin by setting the widths of the  $N/2\dots N-1$  headers with

the same dimensions as the parallel channels, which propagates to an optimized geometry with a minimal footprint, unless the  $N/2\dots N-1$  headers are narrowed further. It should be noted that if the widths of the  $N/2\dots N-1$  headers are increased, all widths will increase, and this technique can be used as a tool to reduce Reynolds numbers throughout the headers and the corresponding minor losses, distribution asymmetry, and parasitic pressure drops illustrated in Section 6. In other applications, we have written algorithms to limit parameters such as Reynolds number or fluidic shear stress throughout the header channels by stipulating that Eq. (8) must be satisfied and flow through all header satisfies the secondary condition. Practically, this is implemented by wrapping the width optimization algorithm detailed later in this section by a similar algorithm stipulating the secondary condition. These applications were equally successful and resulted in alternative, more linear, header shapes unique to these restrictions.

Next, the geometries of the first  $1\dots N/2$  inlet headers are set to satisfy the relation in Eq. (8), which involves increasing their width and/or height relative to the last  $N/2\dots N-1$  inlet headers. Note that if there are an odd number of parallel channels, the middle  $N/2$  inlet header, which is not related to any other, is simply assigned the geometry of the adjacent  $N/2+1$  inlet header.

Since Eq. (9) is far from a simple expression relating  $W$  to  $R/A$ , it is not trivial to fit a universal expression to approximate the set of  $W_i$  for any geometry since there are also dependencies on channel height and length. Rather, we wrote a simple search algorithm to find  $W_i$  for the first  $1\dots N/2$  inlet headers by the following operations:

- (1) For the  $N/2\dots N-1$  inlet headers, calculate the  $R/A$  ratios, and set the target  $R/A$  ratios for the  $1\dots N/2$  inlet headers by Eq. (8). All subsequent steps regard the  $1\dots N/2$  inlet headers.
- (2) Set  $W_i$  equal to zero, and an initial step size of 1 mm.
- (3) Add a step to the initial  $W_i$  and recalculate  $R_i/A_i$  via Eq. (9).
- (4) If the new  $R_i/A_i$  is greater than the result from step (1), add another step increment and repeat step (2).
- (5) If the new  $R_i/A_i$  is less than the target from step (1), take one step back and decrease the step size by a factor of 10. Proceed with step (2) unless the new step size is less than a specified tolerance increment. If the tolerance limit has been reached, compare  $R_i/A_i$  as is to  $R_i/A_i$  with an added tolerance step, and choose the value closest to the target. In this study, we specified the tolerance increment at 0.01 mm to reflect fabrication limits [2].
- (6) Set the  $i$ th outlet header width equal to the  $(N+1-i)$ th inlet header width.

The program described in Section 2.2 was modified to include this search algorithm and solve for both the initial and optimized flow profiles.<sup>1</sup>

#### 2.4. CFD modeling

As a matter of validation, we used COMSOL Multiphysics® 4.3a to conduct CFD simulations of both air and hydrogen flow distributions through Z-type configuration designs. Geometries were constructed within COMSOL as two-dimensional to ensure numerical tractability. To account for this approximation, a volumetric drag term was added to the velocity field ( $\mathbf{u}$ ),  $F_\mu = -12\mu\mathbf{u}/H^2$ . The

<sup>1</sup> We analyzed a 175 channel Z-configuration with an Intel i7-3517U CPU in only 2.625 s CPU time. Moreover, with UNC-Chapel Hill's KillDevil supercomputing cluster running an Intel Xeon X5650 CPU, we analyzed a 1000 channel configuration in 376.060 s of CPU time.

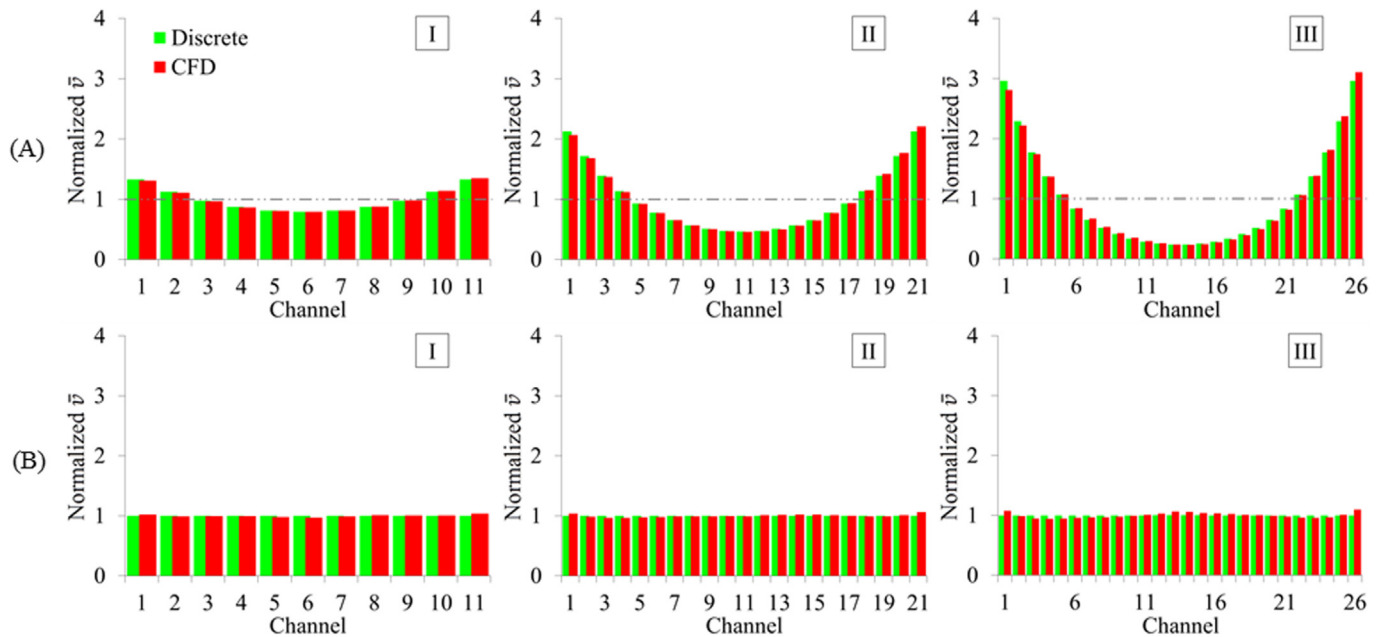


**Fig. 3.** Air flow distributions in (A) initial and (B) optimized geometries I–III calculated via (green) discrete and (red) CFD methods. Dashed lines represent perfectly distributed profiles. (For interpretation of the references to color in this figure legend, the reader is referred to the web version of this article.)

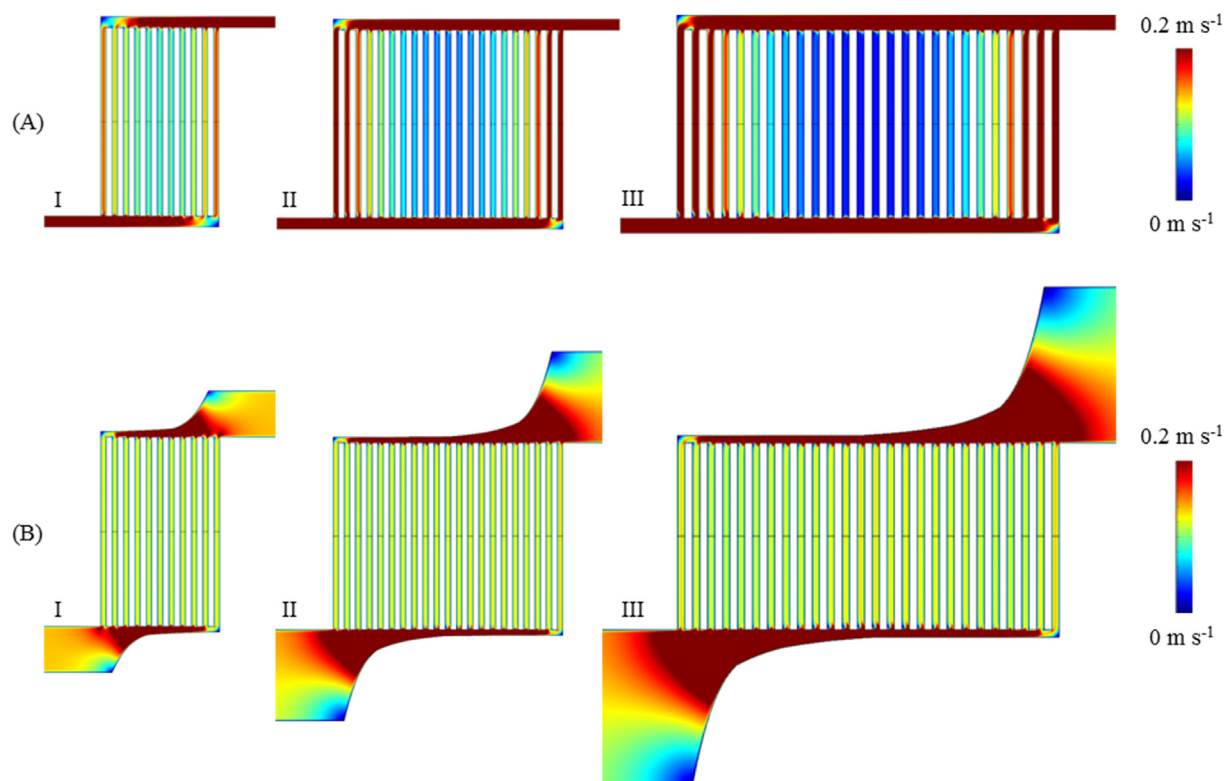


**Fig. 4.** CFD models of air flow in (A) initial and (B) optimized geometries I–III.

validity of this volumetric drag term was affirmed by comparison with a three-dimensional model of geometry I defined in Section 3 (data not shown). Elongated inlets and outlets were used to stabilize flow profiles prior to flow encountering the parallel channels.

A faux internal boundary was drawn across the middle of the parallel channels. This boundary had no effect except to ensure that the meshing algorithm assigned data points along this boundary in each channel, which were used to construct velocity line plots. Solutions were obtained via meshing<sup>2</sup> and solving<sup>3</sup> with custom settings within COMSOL. Excluding points that defined the wall, data was averaged to generate the linear velocity through a parallel channel. To account for small deviations caused by extracting the  $v_i$  data in this manner, sets of  $v_i$  from both discrete and CFD solutions were normalized with respect to the average linear velocity over all  $v_i$ . Pressure drops were calculated using two lines across the inlet and outlet channels, which were directly adjacent to the first and last parallel channel, respectively, to account for the elongated inlets and outlets. The maximum pressure of the inlet line was subtracted from the minimum of the outlet line.

Optimized geometries from discrete solutions in Section 2.3 were constructed within COMSOL by fitting cubic functions through each header segment at the branching tee junctions. This resulted in a smooth transition between the widths, thereby avoiding abrupt changes in fluid flow and minor losses due to sudden contractions. It must be noted that while the cubic function resulted in well distributed flow (see Section 4), this adaptation was empirical. It is entirely plausible that there are alternative methods of fitting the sets of header widths that better match the discrete optimization results. Moreover, potential deviations in the fabrication of these curvatures and their impact on flow distribution warrant future experimental validation.

### 3. Validation

Using both discrete (Section 2.2) and CFD (Section 2.4) methods, we assessed air flow distributions for three published Z-configuration geometries [8,18] that are parameterized in Table 1 and Fig. 2. For comparability, all inlet velocities were set so that the average parallel channel velocity should be  $0.1 \text{ m s}^{-1}$  [8] if perfectly distributed, i.e.,  $V_{in} = (\sum_{i=1}^N a_i)/A_{in} \cdot 0.1 \text{ ms}^{-1}$  (stoichiometry ratio of 1.3 and 3.3 for air and hydrogen, respectively, at a current density of  $0.3 \text{ A cm}^{-2}$ ).

Flow distributions of geometries I–III are shown in Fig. 3A, and CFD velocity surfaces are shown in Fig. 4A. Both sets of  $F_1$  parameters, calculated by Eq. (5) and shown in Table 1, are nearly identical between discrete and CFD results. Additionally, these results coincide with previously published results [8,18], all of which validates the discrete method for these geometries.

### 4. Geometry optimization

We applied the discrete optimization code in Section 2.3 to geometries I–III and adapted the resultant inlet and outlet header widths to the CFD simulations as described in Section 2.4. The  $F_1$  parameters, inlet widths, and percent changes in the pressure

required to drive the system from CFD solutions are shown in Table 2. The optimized flow profiles from discrete and CFD solutions are shown in Fig. 3B, and the CFD velocity profiles are presented in Fig. 4B.

After optimization, we have significantly reduced flow maldistribution in geometries I–III, where the air flow  $F_1$  parameters decreased by 86% on average. Additionally, the parasitic pressure required to drive these optimized geometries is either slightly reduced or essentially unaffected (see Table 2). Thus, this optimization method is effective, simply devised for any given system via the relations in Section 2.3, does not change any geometric parameters of the parallel channels that could affect reaction efficiencies, and offers improved scalability over previous optimization methods [23,24], which is immediately evident from the CPU times in Sections 2.3 and 2.4 that were required to solve for velocity fields and would be further improved by more advanced algorithms than the simplified search algorithm outlined in Section 2.3.

We recognize that the single-phase, steady-state models employed for geometry optimization are limited in scope and do not describe dynamic processes, such as the generation of water droplets/slugs and water purging via hydrodynamic force, that create time-dependent fluctuations in pressure and flow distributions during device operation. Fuel cell flooding remains a critical limitation of parallel systems, such as Z-type geometries, primarily since flow velocities and hydrodynamic forces are significantly reduced (relative to single, serpentine channels) when stoichiometry is conserved [29–32]. The uniform steady-state flow fields illustrated in this section are also necessary to provide uniform hydrodynamic forces for water removal across the entire electroactive surface. As such, the model presented herein functions as a necessary initial step in the development of more complex multi-phase models describing water removal dynamics.

### 5. Minimizing footprint of optimized geometries

As can be seen in Fig. 4, geometry III's footprint increased substantially after optimization. While the optimized header width is on the order of stack manifold headers [33] and likely not an issue for fabrication, it is inevitable that during scale-up, the optimized Z-configuration's footprint could increase beyond tolerable limits or the stack manifolds could become too large. To address this potential issue, we evaluated several avenues by which the leading header widths and total footprint can be minimized without perturbing the uniform flow in the parallel channels.

First, rather than applying the exact widths satisfying Eq. (8), we reduced the headers of the optimized geometry III (Fig. 4B) by different percentages of the optimal widths to determine if we could apply a less exact geometry optimization with a smaller footprint but still yield a uniform flow distribution. The discrete results from applying various percentages of the optimal widths to geometry III are shown in Fig. 5. Note that these percentages regard the increases in widths of the  $1\dots N/2$  headers relative to the widths of the  $N/2\dots N-1$  headers (see Section 2.3). Applying 80% of the

**Table 2**

Optimized geometries' inlet widths (units: mm),  $F_1$  parameters calculated via discrete and CFD analyses, and CFD pressure drops (units: Pa) and their percent decrease relative to initial geometries.

Geometry	Inlet width	Discrete		CFD		
		$F_1$	$F_1$	$\Delta P$	$\Delta\Delta P$ (%)	
I	12.28	0.00	0.06	10.4	-6.8	
II	24.37	0.00	0.09	30.0	-0.3	
III	41.72	0.01	0.14	39.3	-0.6	

<sup>2</sup> The maximum element size, minimum element size, and maximum element growth rate were 0.25 mm, 10.3  $\mu\text{m}$ , and 1.04, respectively; the resolutions of curvature and narrow regions were 0.1 and 16, respectively. The geometries presented herein consisted of approximately 150,000 to 600,000 elements.

<sup>3</sup> Systems were solved using the PARDISO algorithm, the Double-Dogleg nonlinear solver, automatic pseudo-time stepping, and a relative tolerance that was minimized for each geometry to ensure convergence to a unique solution in all cases. For the largest 25-channel geometry, it took 4111 s of CPU time using an Intel i7-3770K processor.

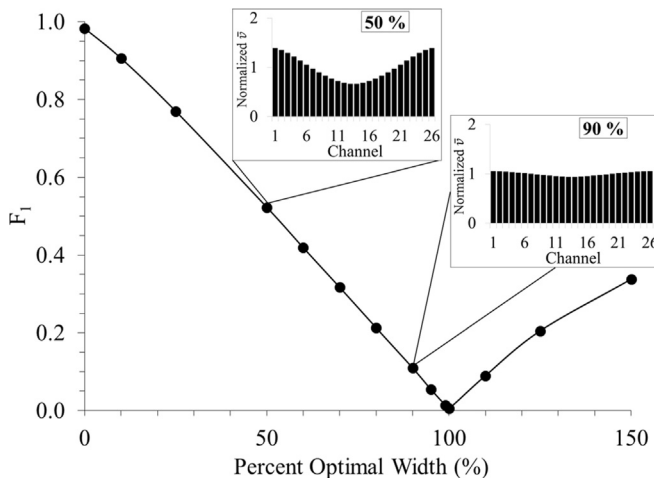


**Fig. 5.** Discrete  $F_1$  parameters for optimizations of geometry III using various percentages of the optimal header widths. The line connecting data points is for illustration only.

optimal widths increased the  $F_1$  parameter from 0.01 to 0.21, but applying 90% resulted in an  $F_1$  of 0.11, which is within the  $\pm 5\%$  deviation that has been previously defined as an acceptable tolerance for flow non-uniformity [22].

Second, discontinuous designs may be applied to optimized geometries in order to reduce the fuel cell's footprint. For example, a discontinuous geometry III is shown in Fig. 6A. It is clear that the

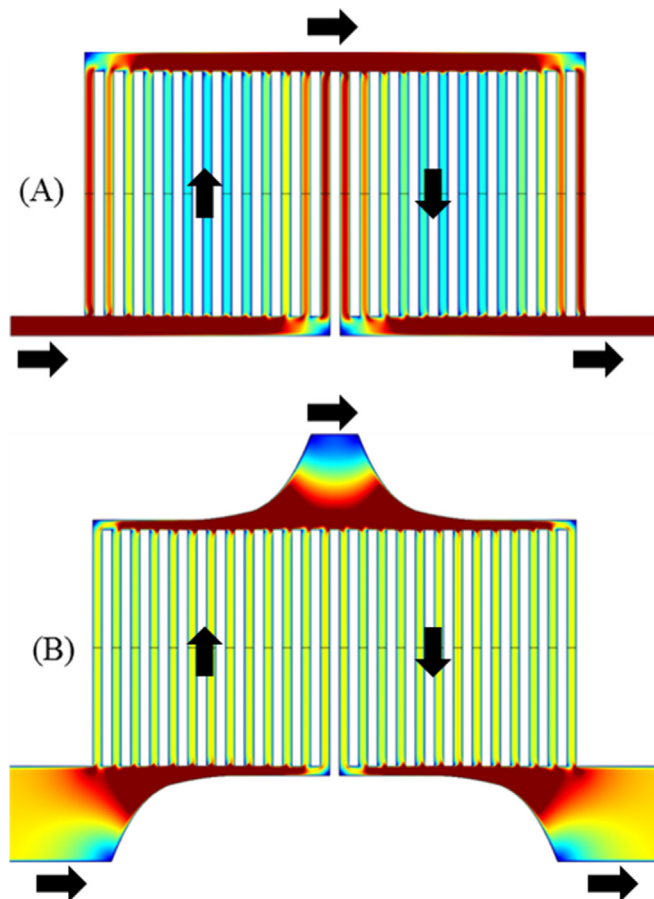


**Fig. 6.** CFD air flow profiles through geometry III in (A) a discontinuous configuration and (B) an optimized discontinuous configuration. The scale bar is shown in Fig. 3.

fundamental maldistribution profiles are still present. Even smaller discontinuous subsets of geometry III would be necessary to further reduce the magnitude of non-uniformity, but again, this optimization technique would result in increased parasitic pressure [3]. However, if we connect optimized subsets of geometry III in a discontinuous fashion (Fig. 6B), maldistribution, pressure, and overall footprint is reduced.

Lastly, channel heights could be increased throughout the entire geometry to minimize the optimized geometry's overall footprint. This necessitates smaller increases in header widths to produce larger decreases in the  $R/A$  ratio in Eq. (9). If geometry III's depth is increased to 1.5 mm, which has been suggested as optimal for hydrogen consumption [25], the optimized leading inlet width then decreases from 41.72 mm to 30.71 mm. This technique is limited because further increases in channel height could reduce reaction efficiency in the parallel channels. Also, changes in the headers' hydraulic diameter and inlet linear velocity may increase Reynolds numbers throughout the inlets, which can cause flow to recirculate at the branching tee junctions and asymmetry in the flow distribution due to the minor losses described in Section 6.

## 6. Minor losses

As mentioned in Section 2.2, resistances within the discrete model only concern major pressure drops to viscous drag. In cases where Reynolds numbers are large enough to induce flow recirculation in the branching tee junctions, the minor loss pressure drops, asymmetric skew in flow distributions, and reagent imbalance between the cathode and anode will not be predicted by this model [3,22,26,27]. We must explicitly state that it is not a trivial task to describe minor losses occurring in branching and combining tee junctions in the algorithms in Section 2.2. Minor effects are a function of the ratio of velocities between the branched and combined flow [26], whereas velocities are individually defined in the  $[V]$  matrix. Including minor effects would require reformulating the entire discrete model.

To demonstrate this issue, we evaluated geometries IV and V that are parameterized in Table 3. Geometry IV was a Z-configuration adapted from channel dimensions optimized for hydrogen consumption by Kumar et al. [25], and geometry V was adapted from a commercially available Z-configuration fuel cell studied by Iranzo et al. [2]. To achieve  $0.1 \text{ m s}^{-1}$  air flow in the parallel channels of geometries IV and V, the Reynolds numbers at the inlets were 129 and 140, respectively, and in Fig. 7, we show flow recirculation developing along the branching tee junctions (experimentally demonstrated by Barreras et al. [19]). These results are contrasted to geometry I in Figs. 4A and 7, where the Reynolds number at the inlet was only 37, and no recirculation was observed.

As the fluid's velocity and Reynolds number decreases along the inlet headers, recirculation and the accompanying minor loss pressure drops decrease in magnitude [26]. Thus, parallel channels farther from the inlet are biased with a lower resistance and faster flow through the parallel channels, thereby modulating the discrete model's parabolic shape to generate the asymmetric distributions shown in Fig. 8A. Thus, for the non-optimized geometry I, no significant air flow distribution asymmetry was observed, and the

**Table 3**

Non-optimized geometric parameters (units: mm) and references for geometries IV–V.

Geometry	Parallel channel properties			Rib width	Inlet width	Inlet height	Ref.	
	Number	Length	Width					
IV	13	37.00	1.50	1.50	0.50	1.50	1.50	[25]
V	25	72.25	2.00	0.80	0.80	2.00	0.80	[2]

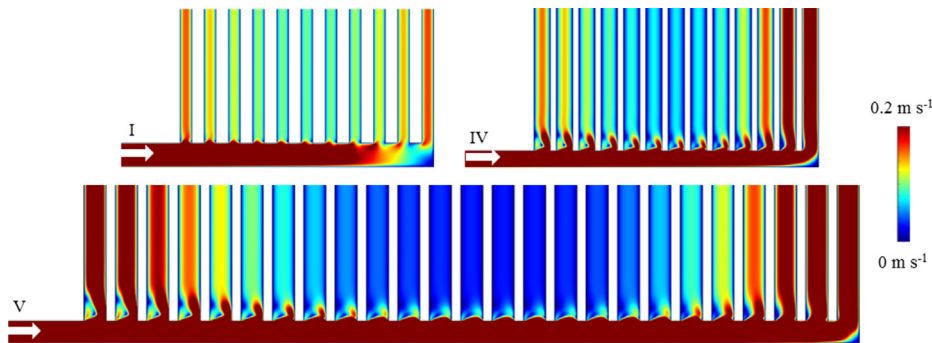


**Fig. 7.** Inlet header velocity profiles showing recirculation and minor losses in geometries I, IV, and V. Arrows indicate direction of flow.

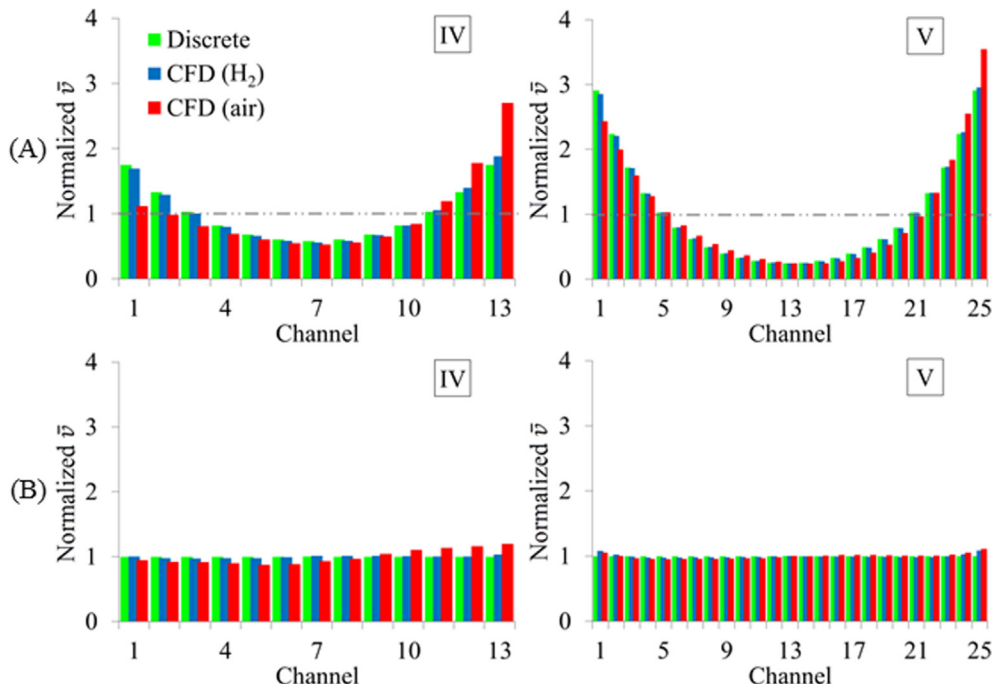


**Fig. 8.** The (A) initial and (B) optimized CFD flow distributions of (red) air and (blue) hydrogen and (green) discrete solution through geometries IV and V. Dashed lines represent perfectly distributed profiles. (For interpretation of the references to color in this figure legend, the reader is referred to the web version of this article.)

non-optimized geometries II and III, which have inlet Reynolds numbers of 70 and 105, respectively, showed slight asymmetry forming in the air flow distributions (see Fig. 3A).

To quantitate these effects, we define a new flow asymmetry parameter:

$$F_2 = \left| \frac{\max\left(v_1 \dots v_{N/2}\right) - \max\left(v_{N/2} \dots v_N\right)}{\max(v_1 \dots v_N)} \right| \quad (10)$$

In all discrete calculations,  $F_2$  will be zero as the flow distribution is always symmetric. But in CFD simulations,  $F_2 \rightarrow 1$  as asymmetry and minor losses become more problematic. For geometries IV and V, both  $F_1$  and  $F_2$  parameters are shown in Table 4 along with CFD pressure drops. As a note, geometries I, II, and III in Fig. 4A have air flow  $F_2$  parameters of 0.03, 0.07, and 0.10, respectively.

Hydrogen flow profiles are less skewed and more closely match discrete results since hydrogen's kinematic viscosity and Reynolds

numbers are an order of magnitude less than air's. As noted previously, this creates reagent imbalance between the cathode and anode that can negatively impact a fuel cell's efficiency [3]. As expected, hydrogen flow  $F_2$  parameters for these geometries are <0.01 for all cases.

Even though these minor losses are not described in the discrete model detailed in Section 2.2 or the optimization method in Section 2.3, the increased header widths in optimized geometries inadvertently reduce these minor losses by reducing Reynolds numbers due to slower reagent flow, which outweighs increasing hydraulic diameters. For example, after optimizing geometries IV and V,

**Table 4**

Non-optimized  $F_1$  parameters from discrete and CFD analyses, and CFD air and hydrogen flow distribution  $F_2$  parameters and pressure drops (units: Pa).

Geometry	Discrete	CFD ( $H_2$ )			CFD (air)		
	$F_1$	$F_1$	$F_2$	$\Delta P$	$F_1$	$F_2$	$\Delta P$
IV	0.67	0.70	0.10	2.2	0.80	0.59	5.7
V	0.92	0.92	0.03	21.2	0.93	0.31	48.0

**Table 5**

Optimized geometries' inlet widths (units: mm),  $F_1$  parameters calculated via discrete and CFD analyses, and CFD  $\Delta P$  pressure drops (units: Pa) and their percent decrease relative to initial geometries.

Geometry	Inlet width	Discrete		CFD ( $H_2$ )				CFD (air)			
		$F_1$	$F_2$	$F_1$	$F_2$	$\Delta P$	$\Delta\Delta P$ (%)	$F_1$	$F_2$	$\Delta P$	$\Delta\Delta P$ (%)
IV	9.86	0.00	0.06	0.02	1.2	-46	0.27	0.21	2.7	-53	
V	41.23	0.00	0.10	0.01	11.2	-47	0.14	0.05	23.7	-51	

pressures were reduced to about half as the minor loss pressure drops lessened (Table 5). The  $F_2$  parameters of geometries I–III were all reduced to 0.02 after optimization, and these asymmetry parameters of geometries IV and V were also reduced, albeit not to the same extent. As mentioned in Section 2.3, rather than constrain optimization results by minimized footprint (by restraining the  $N/2\dots N-1$  headers to the parallel channel width), it is quite straightforward to sequentially increase the  $N/2\dots N-1$  headers until flow through the optimized corresponding header has a Reynolds number less than a specified value, such as 100.

## 7. Conclusions

Uniform delivery of reagents to the Z-configuration's parallel channels is imperative for optimum performance of a fuel cell stack [2–5,7–20]. We modified a simple discrete method to assess flow maldistribution and deduced a mathematical relationship for increasing header widths to optimize the flow distribution. We have shown the accuracy of the discrete method, the success of optimization at reducing flow maldistribution, and the reduction of parasitic minor loss pressure drops and the corresponding flow distribution asymmetry. In all of these optimizations, the parallel channel's geometry, which is often already optimized for reaction efficiency, is not altered, and solutions are obtained with computational ease. To the best of our knowledge, this represents the first time a model has been described to curb flow maldistribution that is universally applicable to all Z-type configurations of planar fuel cells [22]. Furthermore, this research is equally significant in the design of fuel cell stack manifolds, where reagent delivery between layers of the stack exhibits similar maldistribution [34].

Water management was not addressed in this manuscript and remains a critical issue for parallel PEM fuel cells. The multi-phase models [31,35] and empirical measurements [29,36] that are required to address water management in these optimized geometries, especially with respect to the water dynamics occurring in the optimized header channels, are currently under investigation. In alternative fields of study, such as microfluidics, where large scale Z-configuration networks are needed for liquid delivery [37–39], this optimization method is immediately applicable.

## Acknowledgments

The authors would like to thank the University Cancer Research Fund (University of North Carolina at Chapel Hill) for partial financial support of this work and the ITS Research Computing Center (University of North Carolina at Chapel Hill) for access to the KillDevil supercomputing cluster.

## References

- [1] X. Li, I. Sabir, Int. J. Hydrogen Energy 30 (2005) 359–371.
- [2] A. Irazo, M. Muñoz, F. Rosa, J. Pino, Int. J. Hydrogen Energy 35 (2010) 11533–11550.
- [3] S. Maharudrayya, S. Jayanti, A.P. Deshpande, J. Power Sources 157 (2006) 358–367.
- [4] D. Tondeur, Y. Fan, J.-M. Commene, L. Luo, Chem. Eng. Sci. 66 (2011) 2568–2586.
- [5] A.P. Manso, F.F. Marzo, J. Barranco, X. Garikano, M. Garmendia Mujika, Int. J. Hydrogen Energy 37 (2012) 15256–15287.
- [6] J. Wang, Int. J. Hydrogen Energy 33 (2008) 6339–6350.
- [7] J. Wang, Int. J. Hydrogen Energy 35 (2010) 5498–5509.
- [8] S. Maharudrayya, S. Jayanti, A.P. Deshpande, J. Power Sources 144 (2005) 94–106.
- [9] T. Dey, P.C. Ghosh, D. Singdeo, M. Bose, R.N. Basu, Int. J. Hydrogen Energy 36 (2011) 9967–9976.
- [10] H.M. Jung, W.Y. Lee, J.S. Park, C.S. Kim, Int. J. Hydrogen Energy 29 (2004) 945–954.
- [11] G. Karimi, J.J. Baschuk, X. Li, J. Power Sources 147 (2005) 162–177.
- [12] R.J. Kee, P. Korada, K. Walters, M. Pavol, J. Power Sources 109 (2002) 148–159.
- [13] J.-H. Koh, H.-K. Seo, C.G. Lee, Y.-S. Yoo, H.C. Lim, J. Power Sources 115 (2003) 54–65.
- [14] Z. Ma, S.M. Jeter, S.I. Abdel-Khalik, J. Power Sources 108 (2002) 106–112.
- [15] Z. Ma, S.M. Jeter, S.I. Abdel-Khalik, Int. J. Hydrogen Energy 28 (2003) 85–97.
- [16] S. Shimparee, J.W. Van Zee, Int. J. Hydrogen Energy 32 (2007) 842–856.
- [17] Y. Sung, J. Power Sources 157 (2006) 395–400.
- [18] W. Zhang, P. Hu, X. Lai, L. Peng, J. Power Sources 194 (2009) 931–940.
- [19] F. Barreras, A. Lozano, L. Valiño, C. Marín, A. Pascau, J. Power Sources 144 (2005) 54–66.
- [20] D. Martín, D.M. Guinea, B. Moreno, L. González, M.C. García-Alegre, D. Guinea, Int. J. Hydrogen Energy 32 (2007) 1572–1581.
- [21] M. Secanell, J. Wishart, P. Dobson, J. Power Sources 196 (2011) 3690–3704.
- [22] L.G.J. de Haart, M. Spiller, Fuel cells – solid oxide fuel cells | gas distribution, in: G. Jürgen (Ed.), Encyclopedia of Electrochemical Power Sources, Elsevier, Amsterdam, 2009, pp. 77–87.
- [23] N. Guo, M.C. Leu, U.O. Koylu, Int. J. Hydrogen Energy 38 (2013) 6750–6761.
- [24] R. Manikanda Kumaran, G. Kumaraguruparan, T. Sornakumar, Appl. Therm. Eng. 58 (2013) 205–216.
- [25] A. Kumar, R.G. Reddy, J. Power Sources 113 (2003) 11–18.
- [26] J. Wang, Chem. Eng. J. 168 (2011) 1331–1345.
- [27] B. Chernyavsky, P.C. Sui, B.S. Jou, N. Djilali, Int. J. Hydrogen Energy 36 (2011) 7136–7151.
- [28] W.M. Kays, M.E. Crawford, Convective Heat and Mass Transfer, 2d ed., McGraw-Hill, New York, 1980.
- [29] D. Spernjak, A.K. Prasad, S.G. Advani, J. Power Sources 195 (2010) 3553–3568.
- [30] X.C. Wang, B.A. Zhou, J. Power Sources 196 (2011) 1776–1794.
- [31] S.G. Kandlikar, E.J. See, M. Koz, P. Gópalan, R. Banerjee, Int. J. Hydrogen Energy 39 (2014) 6620–6636.
- [32] M.B. Ji, Z.D. Wei, Energies 2 (2009) 1057–1106.
- [33] C.-H. Chen, S.-P. Jung, S.-C. Yen, J. Power Sources 173 (2007) 249–263.
- [34] W.L. Huang, Q. Zhu, J. Power Sources 178 (2008) 353–362.
- [35] H.Y. Kim, S. Jeon, M. Song, K. Kim, J. Power Sources 246 (2014) 679–695.
- [36] R. Banerjee, S.G. Kandlikar, J. Power Sources 247 (2014) 9–19.
- [37] J.M. Jackson, M.A. Witek, M.L. Hupert, C. Brady, S. Pullagurla, J. Kamande, R.D. Aufforth, C.J. Tignanelli, R.J. Torphy, J.J. Yeh, S.A. Soper, Lab. Chip 14 (1) (2014) 106–117.
- [38] J.W. Kamande, M.L. Hupert, M.A. Witek, H. Wang, R.J. Torphy, U. Dharmasiri, S.K. Njoroge, J.M. Jackson, R.D. Aufforth, A. Snavely, J.J. Yeh, S.A. Soper, Anal. Chem. 85 (19) (2013) 9092–9100.
- [39] A.A. Adams, P.I. Okagbare, J. Feng, M.L. Hupert, D. Patterson, J. Gottert, R.L. McCarley, D. Nikitopoulos, M.C. Murphy, S.A. Soper, J. Am. Chem. Soc. 130 (2008) 8633–8641.